REVIEW OF SCIENTIFIC INSTRUMENTS **84**, 123705 (2013)

An interferometric scanning microwave microscope and calibration method for sub-fF microwave measurements

T. Dargent,[1] K. Haddadi,[1] T. Lasri,[1] N. Clément,[1] D. Ducatteau,[1] B. Legrand,[1]
H. Tanbakuchi,[2] and D. Theron[1,a)]
[1]*Institut d'Electronique, de Microélectronique et de Nanotechnologie, CNRS UMR 8520/University of Lille 1, Avenue Poincaré, CS 60069, 59652 Villeneuve d'Ascq, France*
[2]*Agilent Technologies, 1400 Fountaingrove Parkway, Santa Rosa, California 95403, USA*

(Received 17 July 2013; accepted 3 December 2013; published online 23 December 2013)

We report on an adjustable interferometric set-up for Scanning Microwave Microscopy. This interferometer is designed in order to combine simplicity, a relatively flexible choice of the frequency of interference used for measurements as well as the choice of impedances range where the interference occurs. A vectorial calibration method based on a modified 1-port error model is also proposed. Calibrated measurements of capacitors have been obtained around the test frequency of 3.5 GHz down to about 0.1 fF. Comparison with standard vector network analyzer measurements is shown to assess the performance of the proposed system. © *2013 AIP Publishing LLC*. [http://dx.doi.org/10.1063/1.4848995]

I. INTRODUCTION

Electrical characterization at the nanoscale is a challenge for beyond CMOS investigations and for understanding the electronic properties of nanomaterials and nanodevices. However, due to their small size, nanodevices exhibit high impedance in comparison with the 50 Ω reference of standard measurement equipment such as vector network analyzer (VNA).[1] Moreover, at this scale, VNAs are commonly associated to a probe station that is not suited for direct visualization and probing of nano-objects. To overcome these limitations, several groups are developing techniques and related instrumentation, based on different methods. For instance, integration of nano-objects in RF circuits have been proposed.[2] Many techniques combine microwave measurements and atomic force microscopy (AFM) for imaging purposes[3–5] or for quantitative characterization of electromagnetic properties.[6–9] Buried structures can be detected with good spatial resolution using millimeter wave frequencies.[10] Some techniques use resonant cavities for enhancing the measurement sensitivity.[8] Recently, a large activity has been developed for quantitative measurements of capacitances down to 100 aF,[11,12] or doping[13] by Scanning Microwave Microscopy (SMM). By coupling the devices to be measured to the VNA with an AFM-like probe, it is possible to contact nano-objects allowing simultaneous topography imaging and electrical characterization. However, a huge impedance mismatch remains between the reference impedance of the VNA $Z_C = 50\ \Omega$ and the high impedance Z_{DUT} of the device under test (DUT). Since the reflection coefficient $\Gamma_{DUT} = a_{ref}/a_{inc}$ (Figure 1(a)) is related to the impedance Z_{DUT} by $\Gamma_{DUT} = (Z_{DUT} - Z_C)/(Z_{DUT} + Z_C)$ the measurement resolution of the VNA can be estimated by expressing the relative variation of the impedance to the reflection coefficient variation: $(\Delta Z_{DUT}/Z_{DUT})_{VNA} = [(Z_{DUT} + Z_C)^2/2Z_{DUT}Z_C]\Delta\Gamma_{DUT}$. The smallest distinguishable variation of the DUT impedance is therefore not only limited by the resolution of the VNA receiver given by its noise floor, but also by the value Z_{DUT}. Actually, for high values of Z_{DUT}, ΔZ_{DUT} increases with Z_{DUT}^2, which means that the resolution on the determined value of Z_{DUT} is strongly degraded as Z_{DUT} increases. To overcome this limitation, Agilent Technologies has introduced a commercial SMM (named AT-SMM) for microwave quantitative measurements in the frequency range 1–20 GHz.[14] This AT-SMM is based on an AFM associated to a traditional VNA. An RF cable is connected between the measurement port of the VNA and a conductive AFM tip. The incident microwave signal is then injected to the DUT through the AFM tip and a reflected signal is measured by the VNA. To reduce the impedance mismatch between the 50 Ω impedance of the VNA and the impedance to be measured, the AFM probe holder (or nosecone) includes a 50 Ω lumped resistor shunt[11] (see Figure 1(b)). Consequently, most of the incident signal is absorbed by the 50 Ω resistor, bringing the reflected signal close to 0. The set-up includes also an additional module named DPMM (Dopant Profile Measurement Module) mounted on the VNA that contains amplifiers. This is schematically shown in Figure 1(b) and in Ref. 11. These amplifiers increase both incident and reflected signal amplitudes, which result in an enhanced sensitivity and in the possibility to distinguish between close values of DUT impedances. It is noticed that a short cable length connects the resistor shunt to the AFM tip. Consequently, the transmission coefficient of such a setup $T_{AT\text{-}SMM}$ defined as a_2/a_1 in Figure 1(b) is theoretically around 0 only for frequencies of operation where this cable length is a multiple of a half guided wavelength. It is given by $T_{AT-SMM} = -A_{AT-SMM}Z_C/(2Z_{DUT} + Z_C)$, where $A_{AT\text{-}SMM}$ is a complex term that takes into account the gains of the amplifiers including those in the DPMM, the losses and phase-shifts in the cables and couplers. The module of $A_{AT\text{-}SMM}$ is 24 dB at

[a)]Author to whom correspondence should be addressed. Electronic mail: didier.theron@iemn.univ-lille1.fr

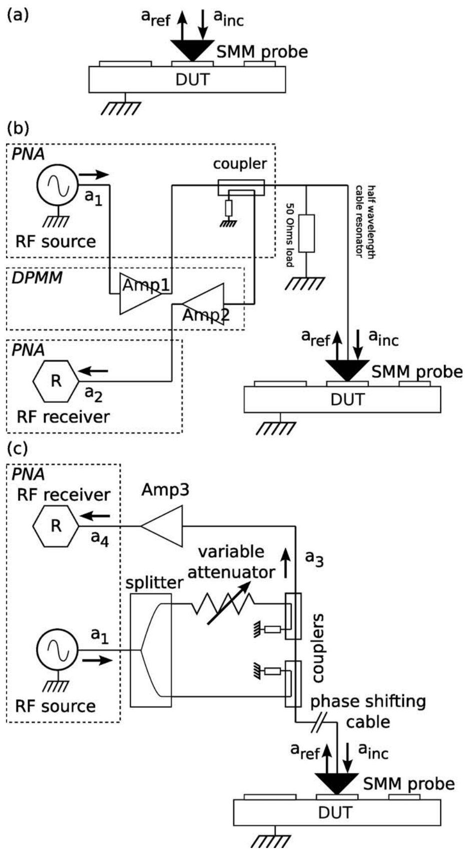

FIG. 1. (a) Definitions of the incident and reflected signal on the DUT. (b) Schematic of the Agilent Technologies SMM set-up integrating a 50 Ω resistor shunt and a half wavelength resonator in the probe holder. (c) Proposed set-up integrating an adjustable microwave interferometer based on a Mach-Zehnder configuration.

3.9 GHz. In other words, for large values of DUT impedance, the $T_{AT\text{-}SMM}$ parameter measured by the VNA with the Agilent Technologies SMM is about $T_{AT-SMM} = -A_{AT-SMM}Z_C Y_{DUT}/2$ where $Y_{DUT} = 1/Z_{DUT}$. With this transformation, the relative variation of the DUT impedance relative to the $T_{AT\text{-}SMM}$ parameter variation becomes: $(\Delta Z_{DUT}/Z_{DUT})_{AT-SMM} = [(2Z_{DUT} + Z_C)^2/2Z_{DUT}Z_C A_{AT-SMM}]\Delta T_{AT-SMM}$. In order to compare the measurement resolution of the VNA and the AT-SMM, we have to consider the ratio between ΔT_{AT-SMM} and $\Delta\Gamma_{DUT}$. Since Γ_{DUT} is measured on the port of the VNA and T_{AT-SMM} using the receiver input, an additional coefficient C_R of 13 dB has to be taken into consideration due to the coupler internal to the VNA located between the port and the receiver connection: $\Delta T_{AT-SMM}/\Delta\Gamma_{DUT} = 1/C_R$. For Z_{DUT} much larger than Z_C, we have $(\Delta Z_{DUT}/Z_{DUT})_{AT-SMM}/(\Delta Z_{DUT}/Z_{DUT})_{VNA} = 4/(C_R A_{AT-SMM})$. Therefore, the advantage of the AT-SMM for high-resolution measurements of large DUT impedance comes from the 50 Ω shunt allowing the amplification of the reflected signal by the gain factor $A_{AT\text{-}SMM}$.

However, this technique has some intrinsic limitations. If the amplifier allows a better separation between signals coming from close impedances compared to a direct measurement with a VNA, it reduces the range of measurable impedances. Indeed, the AT-SMM must be used for measuring transmission coefficients $T_{AT\text{-}SMM}$ near zero that is to say for very high impedance Z_{DUT} in parallel to the 50 Ω resistor shunt. The resistor shunt that is not exactly 50 Ω and the added cable for connection to the VNA lead to measured reflection coefficient in the reduced range of −20 to −25dB[11] although one can note that VNAs present dynamic measurement ranges higher than 100 dB. The sensitivity is highly dependent on the cable length between the AFM tip and the 50 Ω resistor. Nevertheless, the short length of the cable limits severely the frequencies of operation to single measurements spaced by a few GHz.

Here, we introduce a modified SMM technique using an adjustable interferometer to be connected between the VNA and the AFM tip. The resulting system combines multiple advantages: (i) a better measurement resolution compared to the direct VNA technique, (ii) a greater range of measurable impedances, and (iii) an extended set of operation frequencies compared to the commercial Agilent Technologies SMM.

II. EXPERIMENTAL SET-UP

The proposed set-up, including the adjustable interferometer (ITF) is shown schematically in Figure 1(c). As can be seen, the interferometer is quite similar to a Mach-Zehnder configuration. The interferometer is built up with a coaxial power divider, two coaxial hybrid couplers associated to an active variable attenuator. The VNA source provides the incident signal, a_1, which is split into two parts. One part feeds the AFM tip through a coupler and is then reflected back by the DUT impedance. The second part of the signal is adjusted in magnitude by the variable attenuator and is then combined to the reflected signal of the DUT inside the second coupler. The resulting a_3 signal is amplified and analyzed the VNA receiver. For a simple understanding of the interferometer, we consider ideal elements. Thus, there is no parasitic reflection and we assume perfect directivities.

Considering at first a reference impedance Z_{REF} as a DUT impedance, the attenuator can be adjusted to cancel the signal a_3 for wavelengths that correspond to destructive interferences between the signals of the two branches of the interferometer. Note that thanks to the attenuator, the interferences can be obtained for any impedance value. So, measurements are theoretically not limited to very high impedance values. Figure 2 shows the measured and calculated interference signal versus frequency between 3.8 and 4 GHz. Two successive interferences are shown. With the cable length used in our set-up, the interference occurs every 98.1 MHz. Although we cannot choose finely the frequency of the interference, it can be set within a range of ±50 MHz because of the long enough phase shifting cable (Figure 1(c)). This characteristic corresponds to a difference of delay of 10.2 ns between the two interferometer branches, which corresponds to an additional length of cable of about 1 m for the branch going to the SMM tip, assuming an average relative dielectric constant of 2.3 in the cables and taking into account the fact that the signal travels this cable twice. This set-up thus offers many more discrete frequency values of

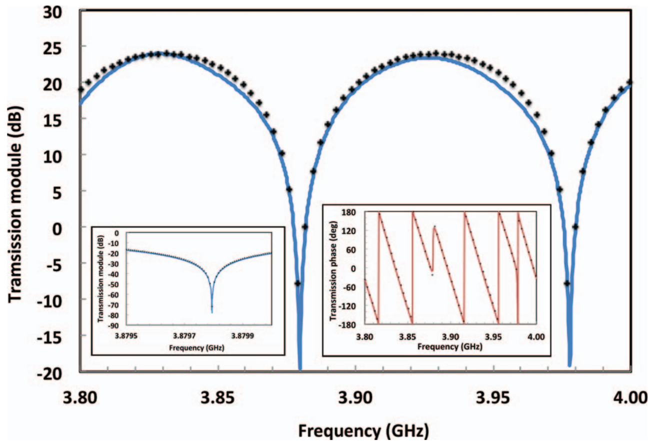

FIG. 2. Interference scheme of the transmission measured by the interferometer setup around between 3.8 and 4 GHz showing the interference repetition every 98.1 MHz. The curves represent measured data. The plus symbols represent calculated values. The right inset shows the phase signal. The left inset shows the detail of the resonance signal after optimum adjustment of the interferometer. For these measurements, an additional attenuator was added just before the VNA receiver in order to measure the whole interference curve dynamics.

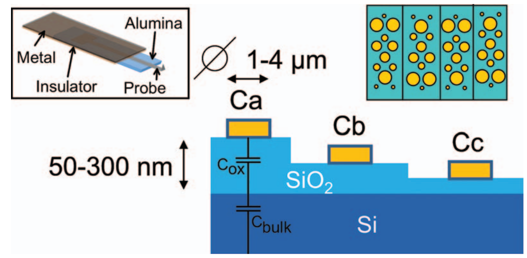

FIG. 3. Calibration kit based on scaled MOS capacitances. The SiO_2 layer is etched to obtain steps with different thickness. The gold electrodes are deposited on the different SiO_2 steps. The top right inset shows the top view of the calibration kit. The top left inset represents the AFM probe configuration with the ground plane (the view is upside down).

measurement than the AT-SMM set-up described before. Note that a phase shifter could be also added in our set-up to obtain a destructive interference at any given frequency, which would allow measurements over a continuous frequency band.

In the conditions where the interference has been obtained for the reference impedance Z_{REF}, the transmission through the interferometer T_{ITF} that is the ratio a_4/a_1 between the incident and received signals (Figure 1(c)) can be calculated from the sum of the signals going though the two branches of the interferometer. It can be written for an arbitrary DUT impedance Z_{DUT} as $T_{ITF} = A(\Gamma_{DUT} - \Gamma_{REF})$, where $\Gamma_{REF} = (Z_{REF} - Z_C)/(Z_{REF} + Z_C)$ is the reflection coefficient of the reference impedance and A is the product of all gains of amplifiers and losses of couplers and attenuators (including phase shifts) in the setup inside or outside the interferometer loop. For impedances Z_{DUT} much higher than Z_c, the measured T_{ITF} will be approximately proportional to $Y_{DUT} - Y_{REF}$ (where $Y_{REF} = 1/Z_{REF}$): $T_{ITF} \cong -2AZ_C(Y_{DUT} - Y_{REF})$. With this simplified modeling, we see that the interferometer will allow measuring DUT admittance values in the range of the reference one with high accuracy, this reference admittance being of arbitrary value. The amplification factor A allows increasing the separation between close values of admittances compared to a direct measurement with a VNA and enhancing the signal-to-noise ratio. High enough amplification will, in particular, allow measuring admittance variations below the resolution of the VNA receiver. Therefore, the amplifier gain will determine the smallest admittance variation $Y_{DUT} - Y_{REF}$ that can be measured. In contrast, as for the AT-SMM technique, amplification will reduce the overall range of measurable admittances since admittances far from Y_{REF} may strongly increase the interference signal, which may result in the saturation of the VNA receiver or nonlinear operation of the amplifiers.

III. CALIBRATION

A. Calibration kit

In order to take into account the imperfections of the interferometer and the VNA, the system must be calibrated. As shown before, accurate measurement is possible only for impedances around a given reference Z_{REF}. So, usual one-port vectorial calibration techniques, that make use of calibration standards well distributed on the Smith chart (such as opens, shorts, lines or 50-Ω load), are not suitable. Calibration standards have to be chosen in the range of the impedances of interest, i.e., around Z_{REF} that is a high impedance value in the context of our study. Huber *et al.*, show a specific calibration kit and a related method to make calibrated measurements with the Agilent Technologies SMM.[11] They obtained a really good matching between the measured and modeled capacitances. More recently, Hoffmann and Wollensack presented results using vectorial calibration.[12] In our study, we developed a calibration procedure based on a modified 1-port error model for the proposed interferometric SMM. The calibration kit used here was developed by Agilent Technologies and MC2-Technologies.[11] It consists of metal-oxide-semiconductor (MOS) capacitors whose values range from 0.1 fF to 10 fF. The MOS capacitors are composed of circular gold electrodes evaporated on silicon dioxide deposited on a P-type silicon substrate of resistivity: 1–3 Ω cm. The calibration kit is depicted in Figure 3. In order to vary the capacitances values, the diameter of the upper gold pad varies from 1 to 4 μm and the SiO_2 thickness ranges from 50 to 300 nm with about 80 nm steps.

B. Modeling

To compute the value of the capacitors, we consider them as two serial capacitances. One C_{ox} comes from the SiO_2 layer and the second C_{bulk} is related to the depleted zone under the SiO_2 and inside the silicon (see Figure 3). C_{ox} is calculated by finite element modeling using COMSOL Multiphysics 4.1. The thickness and areas of the capacitors were estimated from the AFM topography measurements so as to take into account any deviations in size during the fabrication of the calibration kit. The measured thicknesses of the SiO_2 layers were 41 nm, 127 nm, 220 nm, and 301 nm. The measured areas were 1.4 μm^2, 4.7 μm^2, 9.0 μm^2, and 15.6 μm^2.

The series capacitance C_{bulk} is added in order to take into account the depleted region located in the silicon bulk under the oxide. The capacitance was estimated to be proportional to the area of the metallic electrode and inversely proportional to the depleted zone depth according to[15] $C_{bulk} = \varepsilon_0\varepsilon_r S/d_{depl}$ with $d_{depl} = \sqrt{2\varepsilon_0\varepsilon_r\psi_s/qN_A}$. ψ_s represents the voltage drop due to band bending at the Si/SiO_2 interface, N_A is the doping level of the silicon bulk and $\epsilon_0\epsilon_r$ its dielectric constant.

C. Calibration procedure

The impedances Z_{DUT} of the calibration kit capacitors are considered as pure capacitances C. Their reflection coefficient Γ_{DUT} is related to C by

$$\Gamma_{DUT} = \frac{1 - Z_C jC\omega}{1 + Z_C jC\omega}. \tag{1}$$

The microwave characterization is performed by means of the interferometer setup to measure the transmission coefficient T_{ITF}. The newly proposed calibration and measurement methods are detailed as follows:

Step 1: A reference load Z_{REF} with theoretical reflection coefficient Γ_{REF} is used as a DUT. This reference capacitance is realized by setting the AFM probe tip in contact with the sample surface. As the surface of the sample is covered with thick SiO_2 and the probe tip is very small (the tip radius is given to be lower than 20 nm), the reference impedance formed by the tip and the sample can be considered as a very small capacitance much smaller than the capacitances of the calibration kit that have much larger surfaces. With this DUT, the magnitude of the transmission is tuned by means of the variable attenuator of the set-up. The interference signal of Figure 2 is tuned to minimize the transmission at a frequency of interference. This procedure gives the test frequency where the interference signal is minimized. At this frequency, the measured transmission coefficient is around zero, resulting in high measurement sensitivity for impedances around Z_{REF}. The value of Z_{REF} was not calculated and therefore was not used for calibration purposes.

Step 2: For the wave cancellation conditions, a one-port vectorial calibration model is used to make the link between the transmission coefficient T_{ITF} measured by the VNA and the reflection coefficient Γ_{DUT}. Assuming that the setup can be described with a signal flow chart, the model can be given by[16]

$$T_{ITF} = E_{11} + \frac{E_{12}E_{21}\Gamma_{DUT}}{1 - E_{22}\Gamma_{DUT}}. \tag{2}$$

The complex terms E_{11}, $E_{21}E_{12}$, and E_{22} are phenomenological calibration complex parameters that depend on the S-parameters of the interferometer and the microwave probe.

Step 3: Equation (2) can be resolved by a derived SOL (short-open-load) calibration method that makes use of the measurements of the transmission coefficients $T_{ITF,1}$, $T_{ITF,2}$, and $T_{ITF,3}$ of three known standards called $Z_{REF,1}$, $Z_{REF,2}$, and $Z_{REF,3}$ with reflection coefficients $\Gamma_{REF,1}$, $\Gamma_{REF,2}$, and $\Gamma_{REF,3}$. An initial guess of the complex terms E_{11}, $E_{21}E_{12}$, and E_{22} is calculated analytically using three known standards chosen among the 16 capacitances of the calibration kit in order to get a first good fit between the measured and calculated T_{ITF}. Their values will be given in Sec. IV.

Step 4: Nevertheless, the question arises on the number of calibration standards used to solve the problem. Increasing the number of calibration standards leads obviously to a robust and precise calibration task. In the present work, a least-square method using redundantly measured capacitances is used to solve the set of equations (2). This yields an increase of the measurement accuracy and a reduction of the random noise. Now, the impedance to be measured is lossless (only the phase-shift Φ of Γ_{DUT} has to be determined) whereas the VNA measures the magnitude and phase-shift of the transmission coefficient T_{ITF}. Consequently, only the magnitude or the phase-shift of the measured transmission coefficient T_{ITF} is needed to determine the value of the phase-shift of Γ_{DUT} and the related capacitance. In the approach proposed, the interferometric technique enhances the magnitude variations of the reflection coefficient. Consequently, we derive the error function that makes the link between the magnitudes of the measured transmission coefficient T_{ITF} and both the calibration parameters and the phase-shift Φ of the reflection coefficient Γ_{DUT} by the following form

$$|T_{ITF}| - \left| E_{11} + \frac{E_{12}E_{21}e^{j\Phi}}{1 - E_{22}e^{j\Phi}} \right| = 0. \tag{3}$$

The calibration constants are then determined by minimizing the sum of squared residuals of the error function by fitting the model (Eq. (3)) to the measured data. The number of calibration standards can be chosen with respect to both the dynamic capacitances range and the required accuracy expected. The corresponding complex transmission coefficients are acquired for each calibration standard.

Step 5: After the calibration, in order to determine a capacitance value C from the measured T_{ITF} value, we solve the inverse problem to retrieve the phase-shift of Γ_{DUT} and the related capacitance value. The main constraint that occurs in the resolution of the inverse problem is the nonlinear character of equation (3). An efficient balanced nth order polynomial model is then used to express the phase-shift Φ as a function of T_{ITF} and the calibration parameters. The terms are also obtained by a fitting procedure in the transmission coefficient magnitude range of interest. From the measured magnitude of the transmission coefficient T_{ITF}, the phase-shift Φ is determined. The resulting capacitance is then given by

$$C = -\frac{tan(\Phi/2)}{Z_C\omega}. \tag{4}$$

With this approach, we expect to take into account all constant linear parasitic elements. In particular, the AFM probe ends with only one conductor in contact with the device in contrast to common ground-signal-ground probes used for usual RF measurements. The ground is a metal plate located in front of the sample surface (see Figure 3 inset) and therefore the grounds of both sample and probe are connected through a capacitor. Through this calibration procedure, we expect that this coupling capacitance will be partly taken into account.

In Sec. IV, the comparison between measured and theoretical values is used to control the measurement accuracy of our setup.

TABLE I. (a) Calibration constants obtained by one-dimensional interpolation of the model (Eqs. (2) and (3)). (b) Calibration capacitance standards (values from modeling), related Γ_{DUT} parameter phase, related measured magnitude of the transmission $|T_{ITF}|$ and fitted data using E_{11}, $E_{21}E_{12}$, and E_{22} and the model (Eqs. (2) and (3)). The determination coefficient r^2 is 0.998. The frequency is f = 3.5 GHz.

(a)

Calibration parameter	Initial values	Final values
E_{11}	$-3.78 - 0.55i$	$-2.460 + 0.300i$
$E_{21}E_{12}$	$-0.710 \times 10^{-3} + 0.0696i$	$0.032 + 0.005i$
E_{22}	$0.997 - 0.0176i$	$0.987 - 0.003i$

(b)

Number	Capacitance (fF)	Φ (rad)	$\|T_{ITF}\|$	$\|T_{ITF}\|_{\text{fitted}}$	Residual (%)
1	0.17	− 0.000368	0.0266073	0.0277841	− 4.42291
2	0.19	− 0.000418	0.0281838	0.0295407	− 4.814254
3	0.24	− 0.000522	0.0562341	0.0406518	27.709728
4	0.34	− 0.000752	0.0699842	0.0778967	− 11.30619
5	0.50	− 0.001099	0.1437695	0.1397233	2.8143557
6	0.58	− 0.001288	0.1735135	0.1737686	− 0.147003
7	0.76	− 0.001676	0.2166872	0.242716	− 12.01214
8	0.90	− 0.001993	0.3080822	0.298031	3.2625289
9	1.08	− 0.002369	0.3721774	0.3623392	2.6434204
10	1.14	− 0.002515	0.3834129	0.3868928	− 0.907626
11	1.42	− 0.003137	0.462381	0.488677	− 5.687089
12	1.51	− 0.003329	0.5388898	0.519263	3.642095
13	1.81	− 0.003997	0.646398	0.6217593	3.8116963
14	2.17	− 0.004779	0.7396053	0.7348333	0.645209
15	2.43	− 0.005358	0.7897688	0.8135766	− 3.014518
16	3.74	− 0.008247	1.151684	1.148228	0.3000801

IV. RESULTS AND DISCUSSION

A. Measurement of the calibration kit

Measurements were performed at 3.5 GHz with the interferometer setup using a 25PT300A AFM tip from Rocky Mountain Nanotechnology (USA). The RF power sent to the sample was estimated to be lower than −30 dBm. The images were typically scanned over a 60 × 60 μm^2 with 256 pixels at a scan rate of 0.625 line/s. In addition to the topography image, the interferometer setup provides both images of the T_{ITF} parameters in magnitude and phase. The three capacitances used in order to calculate the initial guess of the complex terms E_{11}, $E_{21}E_{12}$, and E_{22} were chosen to have values of 0.34, 2.17, and 3.74 fF among the 16 different capacitance values. For this step, we used the value of ψ_s in the calculation of the series capacitor C_{bulk} as a fit parameter for the total calculated capacitance in order to get a good fit of all the measured capacitances with the theoretical values. The value of ψ_s used for the calculation of C_{bulk} was taken at 0.2 V ± 0.1 V for a doping level of 8 × 10^{15} cm^{-3} estimated from the average resistivity. This corresponds to a series capacitance of 0.33 fF/μm^2. The initial values of E_{11}, $E_{21}E_{12}$, and E_{22} are given in Table I. After fitting of Eq. (3) these parameters were refined and all the Γ_{DUT} and capacitance data were obtained as shown in Table I.

After calibration, the T_{ITF} data extracted from the images are transformed into the capacitances as described above. These capacitances were plotted for comparison with the calculated values (Figure 4(a)). The T_{ITF} parameter image was also processed to form a capacitance image (see inset of Figure 4(a)). The results show good agreement on the whole range going from 0.15 fF to 3.7 fF. The error between the calculated and measured capacitance is in average 5% and is less than 10% for capacitances higher than 0.35 fF.

In order to compare the interferometer with the VNA alone, we performed SMM measurements on the same sample but this time with the VNA port directly connected to the device (without any amplifier nor 50 Ω shunt). In that configuration, the measurements were performed at 3.88 GHz and the RF power sent to the sample was lower than −3 dBm. Due to the bad contrast on the transmission parameter images, we used only the largest capacitances for the calculation of the complex terms E_{11}, $E_{21}E_{12}$, and E_{22}. The results of Figure 4(b) show that the large capacitances could be fitted, but after calibration, the values of the capacitances under 2 fF could not be determined from the calibration.

B. Measurement of the smaller capacitances

In order to further investigate capacitances with smaller values, we realized another series of MOS capacitors. They consisted of a top metal contact evaporated with different thicknesses on a 120 nm SiO_2 layer deposited on a silicon substrate. The top metal contact shape is a square with widths of 1, 0.5, and 0.3 μm. The values of these capacitances are calculated to be 370 aF, 100 aF, and 40 aF. SMM

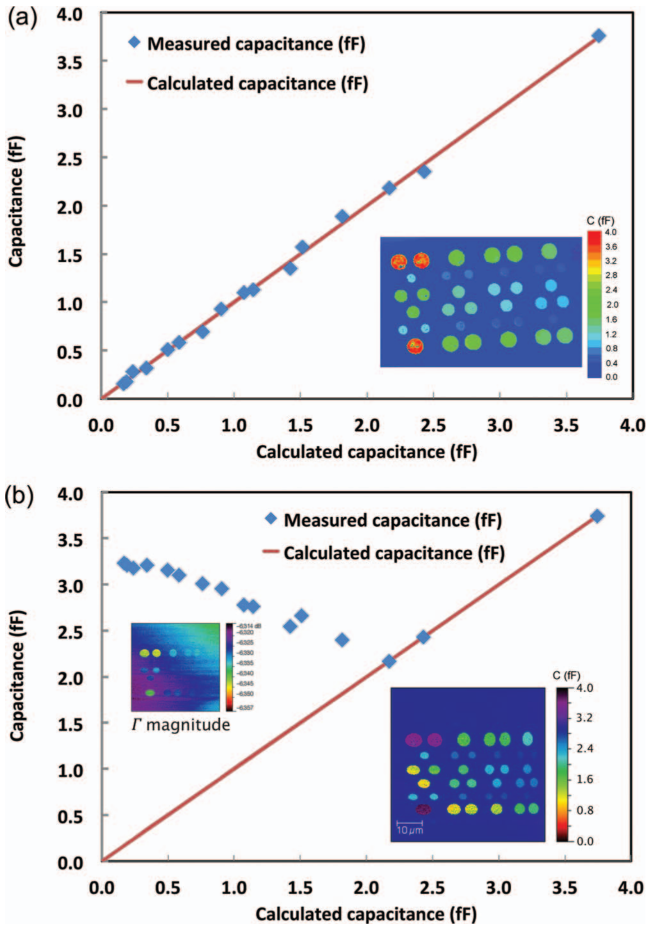

FIG. 4. Capacitances deduced from measurements vs. calculated capacitance values. (a) With the interferometer. The bottom right inset shows the measured capacitance image of the calibration kit. (b) Without the interferometer. The bottom right inset shows the capacitance image obtained after calibration and the top left inset shows the image of the measured Γ parameter magnitude.

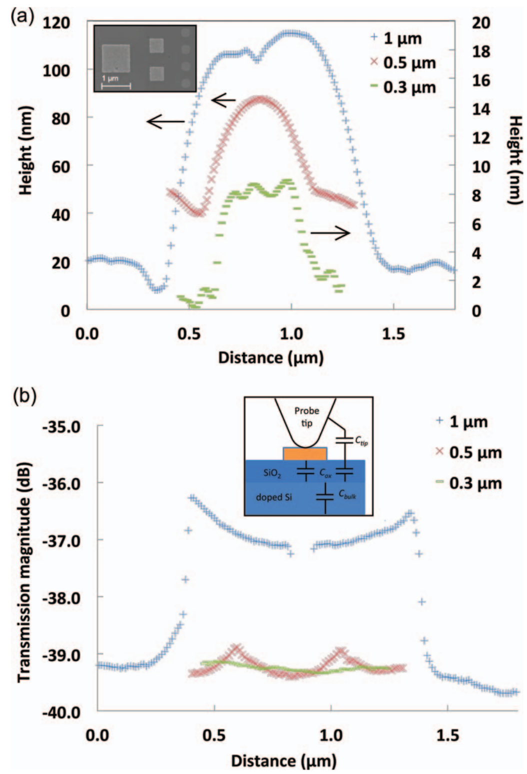

FIG. 5. (a) Profile of the AFM topography image of square capacitances with sides of 1, 0.5, and 0.3 μm. The top left inset shows the top view of the capacitances obtained with scanning electron microscopy. (b) Profile of the transmission parameter magnitude measured across the center of the pads by the interferometer setup. The inset shows the parasitic capacitance C_{tip} coming from the probe tip over the SiO_2/Si substrate.

measurements were scanned over a 23 × 23 μm^2 with 2048 pixels. Figure 5(a) shows the profile of the topography image as well as the SEM top view image of the devices. Figure 5(b) shows the profile of the transmission parameter module measured by the interferometer setup. This figure clearly shows that the measured values are not uniform over the metal surface and that this non-uniformity is more and more important for smaller metal pads. This effect is attributed to the presence of a parasitic capacitance C_{tip} coming from the probe tip over the SiO_2/Si substrate as shown in the insert of Figure 5(b). This capacitance comes in parallel to the metal pad capacitance C_{ox} and starts to have a significant influence for measured capacitances under 100 aF. The decreased value of the measured transmission magnitude near the center of the metal pad is therefore attributed to the screening effect of the metal pad over C_{tip}. Moreover for the smallest pad capacitance of 0.3 μm, no contrast can be seen on the transmission magnitude profile. Therefore, C_{tip} seems to dominate the total measured signal. This shows that the design of the measured devices impacts the value of the impedance measured by our setup. Future work will, therefore, be oriented to other capacitor and tip design in order to better understand the role of the parasitic tip capacitance on the measured values and decrease or de-embed its influence on the measured values.

V. CONCLUSION

In conclusion, we implemented a new Scanning Microwave Microscope using an interferometric set-up for the measurements of very small capacitances. By adjusting the attenuation on one branch of the interferometer, the setup allows a flexible choice of the frequency of interference used for measurements as well as the impedance range where the interference occurs. We implemented calibration based on a 1-port error model to perform calibrated measurements of a set of very small capacitances at 3.5 GHz. The results demonstrate the possibility to measure capacitances down to 0.35 fF with an error estimated to be less than 10%. For capacitances smaller than 0.1 fF, the influence of the parasitic tip capacitance starts to be significant. Further investigation will be performed to reduce and de-embed the influence of this parasitic capacitance.

ACKNOWLEDGMENTS

The Agilent Program for University Research supported this work from 2009 to 2011. The authors would like to acknowledge the IEMN cleanroom and electrical characterization staff for their constant support. The Region

Nord-Pas-de-Calais supported this project under the CPER CIA research project as well as the National Research Agency (ANR) under the programme Equipex (EXCELSIOR project).

[1] P. J. Burke and C. Rutherglen, in *Conference on Precision Electromagnatics Measurements Digest* (IEEE, 2008), pp. 494–495.
[2] L. Nougaret, G. Dambrine, S. Lepilliet, H. Happy, N. Chimot, V. Derycke, and J.-P. Bourgoin, Appl. Phys. Lett. **96**, 042109 (2010).
[3] D. E. Steinhauer, C. P. Vlahacos, S. K. Dutta, F. C. Wellstood, and S. M. Anlage, Appl. Phys. Lett. **71**, 1736 (1997).
[4] A. Imtiaz, S. M. Anlage, J. D. Barry, and J. Melngailis, Appl. Phys. Lett. **90**, 143106 (2007).
[5] A. Tselev, N. V. Lavrik, A. Kolmakov, and S. V. Kalinin, Adv. Funct. Mater. **23**, 2635 (2013).
[6] C. Gao and X.-D. Xiang, Rev. Sci. Instrum. **69**, 3846 (1998).
[7] A. Karbassi, D. Ruf, A. D. Bettermann, C. A. Paulson, D. W. van der Weide, H. Tanbakuchi, and R. Stancliff, Rev. Sci. Instrum. **79**, 094706 (2008).
[8] R. Kleismit, IEEE Trans. Microwave Theory Tech. **54**, 639 (2006).
[9] V. Talanov and A. Schwartz, IEEE Trans. Microwave Theory Tech. **57**, 1224 (2009).
[10] K. Haddadi, D. Glay, and T. Lasri, IEEE Microw. Wirel. Compon. Lett. **21**, 625 (2011).
[11] H. P. Huber, M. Moertelmaier, T. M. Wallis, C. J. Chiang, M. Hochleitner, A. Imtiaz, Y. J. Oh, K. Schilcher, M. Dieudonne, J. Smoliner, P. Hinterdorfer, S. J. Rosner, H. Tanbakuchi, P. Kabos, and F. Kienberger, Rev. Sci. Instrum. **81**, 113701 (2010).
[12] J. Hoffmann and M. Wollensack, in *12th IEEE International Conference on Nanotechnology (IEEE-NANO)* (IEEE, 2012), p. 1.
[13] A. Imtiaz, T. M. Wallis, S.-H. Lim, H. Tanbakuchi, H.-P. Huber, A. Hornung, P. Hinterdorfer, J. Smoliner, F. Kienberger, and P. Kabos, J. Appl. Phys. **111**, 093727 (2012).
[14] F. M. Serry, Agilent Technologies, Application Note 5989-8818EN Rev C (2010).
[15] S. M. Sze, *Physics of Semiconductor Devices*, 2nd ed. (Wiley and Sons Inc., 1981), p. 373.
[16] S. Mason, Proc. IRE **44**, 1144 (1956).